

The Study of the Silicon Detector Response for p-Carbon Polarization Measurements at RHIC

D. Kalinkin^{*1} and D. Smirnov^{†2}

¹Institute for Theoretical and Experimental Physics

²Brookhaven National Laboratory

March 7, 2014

Abstract

At the Relativistic Heavy Ion Collider (RHIC) measurements of the proton beam polarization are conducted by inserting an ultra thin carbon ribbon in the beam and registering the scattered carbon ions with silicon detectors. The polarization value reported by the proton-carbon polarimeters strongly depends on the correct measurement of the energy deposited in the detectors by the recoil products. In this note we present a study of the response of the silicon detectors to α -particles employed to calibrate the detectors.

1 Motivation

The RHIC polarimetry is based on the measurement of the recoil products from elastic scattering of the proton beam on a fixed target in the Coulomb nuclear interference (CNI) energy regime. In this study we focus on the four p-Carbon polarimeters with ultra thin carbon targets which can be moved through the beam. In the current setup the polarization of each proton beam can be measured independently by two p-Carbon polarimeters installed in the “yellow” and “blue” accelerator rings.

During the 2013 run we observed significant changes in the gain in some of the silicon detectors. This change of $\lesssim 20\%$ is worrisome and may cause significant systematic change in the reported polarization values due to a steep slope in the p -Carbon analyzing power within the energy range of interest.

2 Measurement and Results

The detectors produced by the BNL instrumentation group have 12 one-millimeter silicon strips operating under the nominal bias voltage of 110 V. The detector gains are normally monitored by taking calibration runs when there is no beam in the machine. Starting April 3, 2013 the calibration runs were taken automatically at the end of every RHIC store immediately after the beam dump. This approach allowed us to track the changes in detector properties at a more precise level than before. Although we primarily focus on the Run 13 data we also analyzed

^{*}dmitry.kalinkin@gmail.com

[†]d.s@plexoos.com

the data from α -calibration runs in Run 12. The same analysis procedure was performed on Run 12 data as well (see Appendix A). Because alpha runs weren't taken as frequently during Run 12, resulting plots for it don't have as much statistics as the plots for Run 13. The analysis of the data was performed with the `cnipol` package [1].

2.1 Energy calibration with α -particles

For the purpose of polarization measurement we need to measure the energy of the slow carbons ions coming from the fixed target. The calorimetry is done by utilizing the silicon strip detectors introduced above. The energy of the recoil particles can be reconstructed from either the maximum amplitude of the signal or the total charge (i.e. integral) registered by the detector. In general we observe a very good correlation between the maximum amplitude and the integral of the collected charge, therefore, our choice of the former is only set by convention. For the energy calibration purposes we use low intensity ^{241}Am and ^{148}Gd radioactive sources emitting α -particles with fixed energies of $E_{\text{Am}} = 5.486 \text{ MeV}$ and $E_{\text{Gd}} = 3.183 \text{ MeV}$ [2] respectively. The sources are put inside the vacuum of the beam pipe in the direct acceptance of the detectors. In 2012 and 2013 two polarimeters, Y1D and B1U, were supplied with ^{241}Am sources only, while the other two, Y2U and B2D, had, in addition, ^{148}Gd sources installed inside the polarimeter chambers. Prior to 2012 only the americium sources were available for calibration.

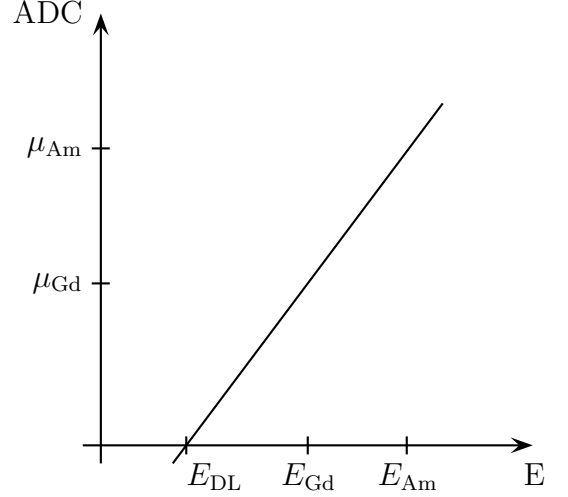


Figure 1: First order calibration curve fitting points corresponding to the two α sources.

The energy of the α -particles is few times higher than that of the carbon ions reaching the detectors. We reduce the output signal by means of attenuators by a factor of five to bring it back to the range where the amplitude can be digitized by the readout electronics. In the absence of the beam we observe clean peaks from the radioactive sources as shown in Figure 15a. The peaks positions are determined using a gaussian function fit.

The current offline analysis is only based on a calibration with the ^{241}Am source. The nominal detector gain g_{Am} is defined as a ratio of the peak position, μ_{Am} , to the E_{Am} energy. This definition completely ignores possible energy losses before the sensitive detector region. This limitation can be overcome to some extent by using a second α -source. With two sources the slope of a linear calibration curve effectively takes into account the unresponsive region of the detector as illustrated with a sketch in Figure 1. This region is referred to as the *dead layer*, and we discuss it in the next section.

Figure 4 shows how the g_{Am} gain developed in time for all four p-Carbon polarimeters. From this we conclude that overall gain was stable on a monthly scale with only few detectors showing up to 10% instabilities in the gain. We also confirm an overall stability by looking at the ratio of the gain estimate for the polarimeters with an additional ^{148}Gd source. These quantities as a function of time are shown on Figure 5.

2.2 Effective dead layer

In our current model of the silicon detector the incident particles are assumed to pass through a region where the detector has zero response as a calorimeter, i.e. the dead layer. Adding a gadolinium alpha source to the setup allows us to put one more calibration point on our cali-

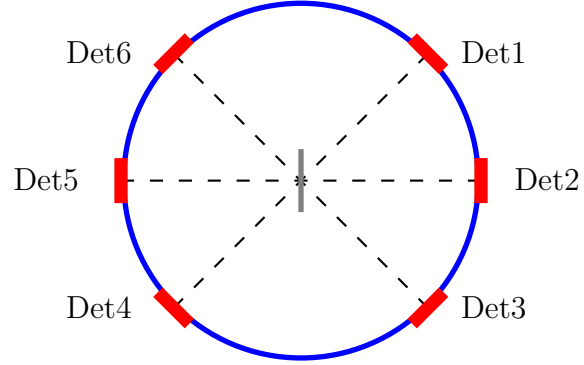


Figure 2: Schematic view of the detector alignment in the plane perpendicular to the beam. Carbon strip target is aligned vertically, detectors are aligned at angles 45° , 90° , 135° to it. The beam points into the figure perpendicularly.

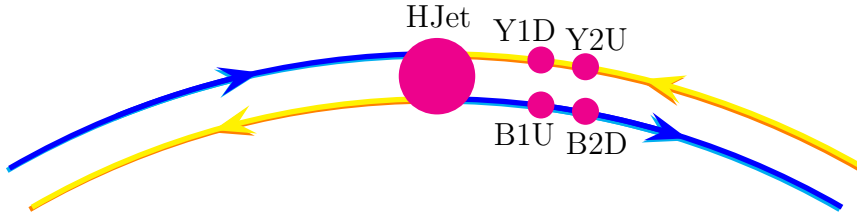


Figure 3: Schematic view of polarimeters placement around IP12.

bration curve (see Figure 1). With the points corresponding to the americium and gadolinium sources we can estimate the thickness of this layer.

The energy where the linear fit intersects the horizontal axis gives us an estimate for the initial energy of incident α -particles which would deposit all of their energy in the dead layer. While this quantity by itself can be used to monitor the stability of the dead layer over time, we also present the result in microns. For the latter, we assume that the detector response to the both incident energies is the same, and we write:

$$\frac{\mu_{Am}}{E_{Am} - E_{Am}^{DL}} = \frac{\mu_{Gd}}{E_{Gd} - E_{Gd}^{DL}}, \quad (1)$$

where μ_{Am} and μ_{Gd} are the mean values of the alpha peaks measured in ADC units, E_{Am} and E_{Gd} are the incident energies of α -particles, and E_{Am}^{DL} and E_{Gd}^{DL} are the energy losses in the dead layer for the respective alpha sources.

The rate at which α -particles loose their energy in the detector changes with the penetration depth. The value of stopping power can be easily derived from the *CSDA range*¹ values available at the ASTAR Database[3].

The original CSDA range data for α -particles is displayed in Figure 6a. If we take CSDA range value for the $E = E_{Am}$ and $E = E_{Gd}$ we will get maximal penetration depths z_{Am}^0 , z_{Gd}^0 . Penetration depth is then calculated as $z_i = z_i^0 - \text{CSDA range}$. Stopping power $-\frac{dE}{dz_i}$ can be then derived from E vs z_i points using simple numerical differentiation formula $\frac{df}{dx} = (f_{i+1} - f_i)/(x_{i+1} - x_i)$. The resulting plot for stopping power versus penetration depth can be seen in Figure 6b. This plot is consistent with the other plot[4] of the same dependency, derived from the data from the same ASTAR Database, but using a different method.

As the dead layer is relatively thin (less than 2 μm) α -particles do not loose a significant fraction of their initial energy and the stopping power is approximately constant over this range. With a linear approximation for the total losses we have:

$$E_{Am}^{DL} \simeq x_{DL} \lambda_{Am} \quad E_{Gd}^{DL} \simeq x_{DL} \lambda_{Gd} \quad (2)$$

with values for the stopping power $\lambda_{Am} = 140 \text{ keV}/\mu\text{m}$ and $\lambda_{Gd} = 190 \text{ keV}/\mu\text{m}$ taken from the plot on Figure 6b at $z = 0$. Combining Equations (1) and (2) we obtain the following formula for the size of the dead layer:

$$x_{DL} = \frac{\mu_{Gd} E_{Am} - \mu_{Am} E_{Gd}}{\mu_{Gd} \lambda_{Am} - \mu_{Am} \lambda_{Gd}} \quad (3)$$

The thickness of the dead layer thus extracted from the all available calibration runs in Run 13 are shown in Figure 8. The average size of the dead layer is estimated to be within 1 to 1.3 μm .

2.3 Bias current

In Figures 5, 7 and 8 there are few measurements before and after the beam session showing much lower spread. This points at beam pickup nature of the variation seen during the beamtime.

One of the work parameters of our silicon detector that we measure is a bias current – current constantly flowing through detector (in this case – set of 12 strips). Current was measured for

¹The *CSDA range* is a very close approximation to the average path length traveled by a charged particle as it slows down to rest, calculated in the continuous-slowing-down approximation. In this approximation, the rate of energy loss at every point along the track is assumed to be equal to the total stopping power. Energy-loss fluctuations are neglected. The CSDA range is obtained by integrating the reciprocal of the total stopping power with respect to energy. – ASTAR Appendix: Significance of Calculated Quantities

each of the six silicon detectors on all polarimeters, measurements were taken each five minutes. Values lie mostly in range from -30 to $0 \mu\text{A}$. It was interesting to see how this current affects calibration characteristics of our detector. For example, it is known that higher bias voltage should decrease size of depleted zone, i.e. decrease size of dead layer. On our plots (Figure 11) we see some weak correlation between dead layer size and bias current.

Much stronger correlation is seen when we compare bias current with gain (Figure 12). Bias current during polarization measurement can differ from the bias current in the time of alpha measurement, so correction to the gain value should be applied.

Additional correlation seen on plots on Figures 12a and 12b corresponds to special set of measurements with varied bias voltage.

2.4 Linearity of the amplifiers

The signal generated in the detector propagates through several stages of amplification. Linearity of the downstream amplifiers can be checked by attenuating the signal in a place on the signal path preceding the amplification, and then comparing the measured reduced amplitude with the expected one properly scaled by a known factor.

The shaper boards have a resistive divider with a multiplexer controlled by software settings. For normal polarization measurements of sub-MeV carbon ions the on-board attenuator is set to 1, i.e. no signal attenuation. During regular alpha measurements the attenuator is set to $1/5$. In this study we check the other two attenuator settings of $1/10$ and $1/3$. The alpha peaks obtained with these attenuator settings are shown in Figure 15 and the mean values corresponding to the gaussian fits are listed in Table 1. Note that with the attenuator setting of $1/3$ the americium peak ends up in the overflow bin as the events are outside of the detector dynamic range. The cumulative effect of a possible non-linearity in the amplified signal is checked by using the relation in which the mean of the peak is expected to scale with the attenuator settings:

$$\lambda_1/\lambda_2 = \mu_1/\mu_2. \quad (4)$$

Table 1: The mean positions of the ^{241}Am and ^{148}Gd α -peaks with different attenuator settings.

Attenuation λ	Alpha Run Id	Am Mean, ADC	Gd Mean, ADC
$\frac{1}{10}$	atten_1_over_10.yel2.alpha0	77.0 ± 0.7	44.2 ± 0.4
$\frac{1}{5}$	13_310713.yel2.alpha0	154.9 ± 2.7	88.9 ± 1.5
$\frac{1}{3}$	atten_1_over_3.yel2.alpha0	—	149.4 ± 2.5

This effect relative to one of the attenuator settings is then simply defined as $\Delta l = \frac{\lambda_1 \mu_2}{\lambda_2 \mu_1} - 1$. For the three pairs of measurements we calculate very small deviations from the linear Equation (4).

$$\frac{154.9}{77.0 \times 2} - 1 = 0.6\% \quad \frac{88.9}{44.0 \times 2} - 1 = 0.6\% \quad \frac{149.4 \times 3}{88.9 \times 5} - 1 = 0.8\% \quad (5)$$

3 Conclusions

Based on the analysis presented in this note we establish that the changes in the bias currents in our silicon detectors heavily depend on the beam activity in RHIC. At the moment, we do not see that the bias current correlates with the beam intensity but in further studies we

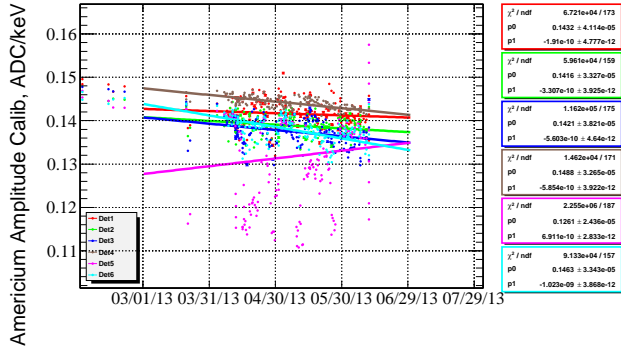
plan to investigate if other beam or machine parameters have direct impact on the detectors (Figure 13).

We observe a strong correlation between the gain and the bias current. This variation goes as high as $\approx 20 - 40\%$ on the operational bias current span (Figure 12). We believe that the entire analysis may benefit from a correction addressing such time-dependant fluctuations. However, implementing it at the moment is not feasible due to the fact that the bias current measurements are taken only once each five minutes. This is enough to determine the average bias current for 20-minute long alpha runs, but a regular sweep polarization measurement takes only a few seconds. It is not unusual for the bias current to change significantly just after the measurement (Figure 14). We believe that it would be better to have more frequent bias current measurements in the future.

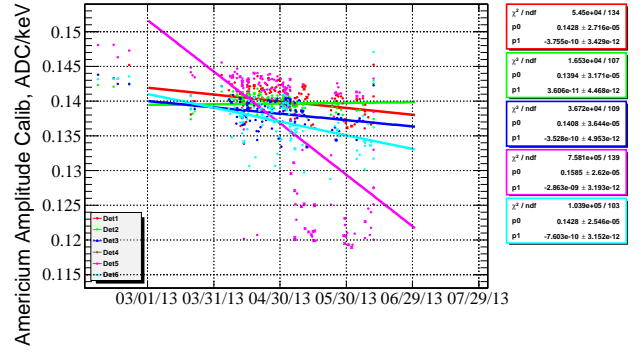
The presence of the two α -sources in the polarimeters allowed us to find a correction for the effective detector gain by taking into account dead layer energy losses. We find this correction (Figure 5) to be at $\approx 5\%$ level with respect to the nominal calibration procedure with one radioactive source. In addition, we estimate the thickness of the effective dead layer to be $\approx 80 \mu g/cm^2$. This number disagrees with the value extracted from the nominal “banana” fit to the carbon data where the dead layer is estimated to be $\approx 35 \mu g/cm^2$.

Comparing the detector gains measured before and after the beam time we conclude that there was no significant radiation damage of the detectors.

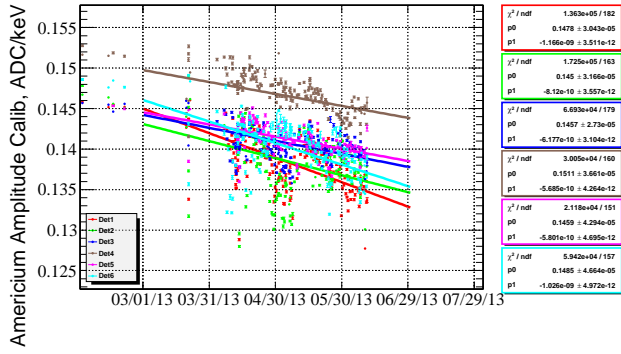
A similar study has been performed for the 2012 data. The corresponding plots can be found in Appendix A.



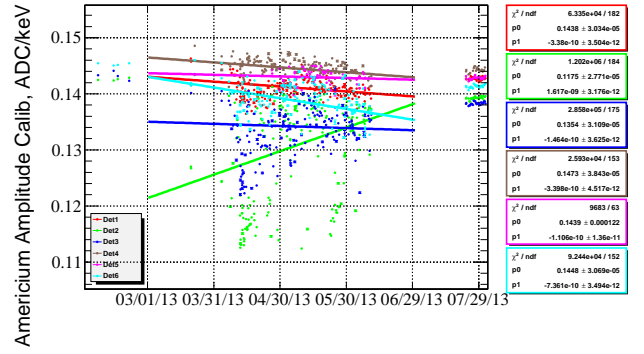
(a) B1U



(b) Y1D

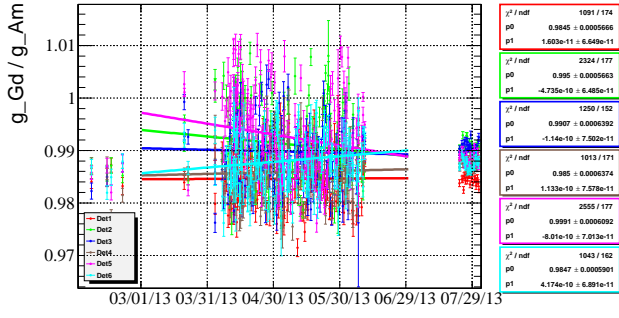


(c) B2D

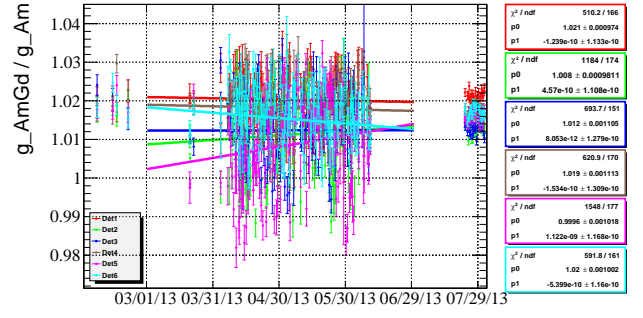


(d) Y2U

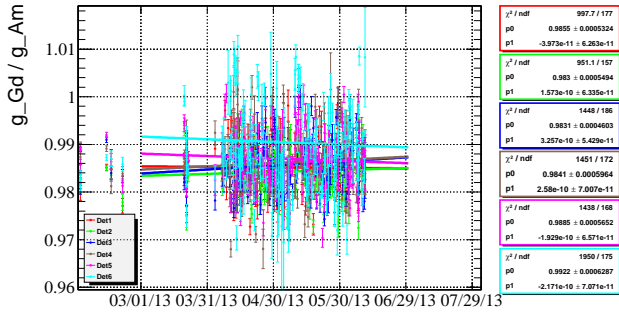
Figure 4: Time dependence of the detector gain g_{Am} as measured with α -particles emitted by the ^{241}Am source. Colors represent individual detectors.



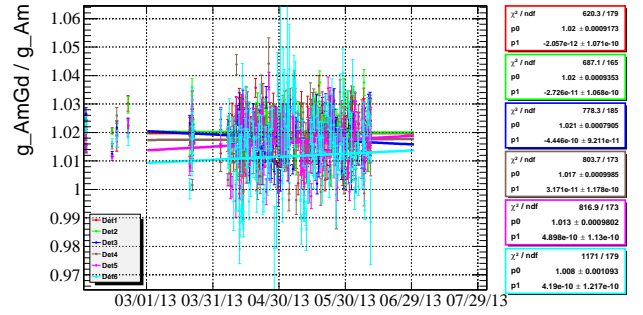
(a) Time dependence of the ratio of the gains, $g_{\text{Gd}}/g_{\text{Am}}$, independently measured with ^{148}Gd and ^{241}Am sources for **Y2U** polarimeter.



(b) Time dependence of the ratio of the gain measured with both ^{241}Am and ^{148}Gd sources to the nominal gain measured with only the ^{241}Am source for **Y2U** polarimeter.

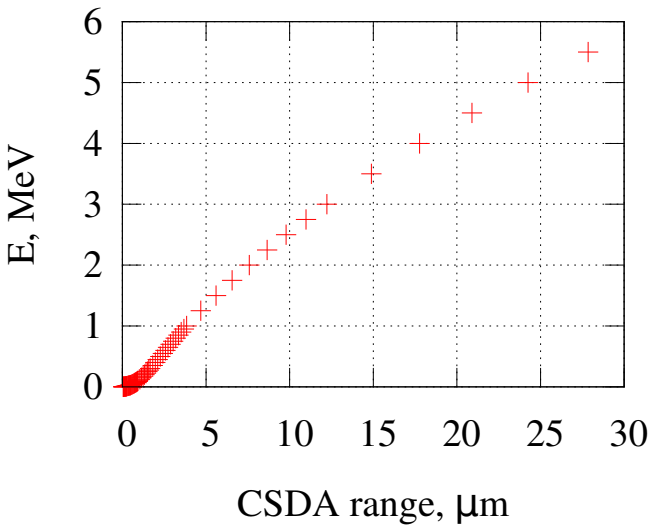


(c) Time dependence of the ratio of the gains, $g_{\text{Gd}}/g_{\text{Am}}$, independently measured with ^{148}Gd and ^{241}Am sources for **B2D** polarimeter.

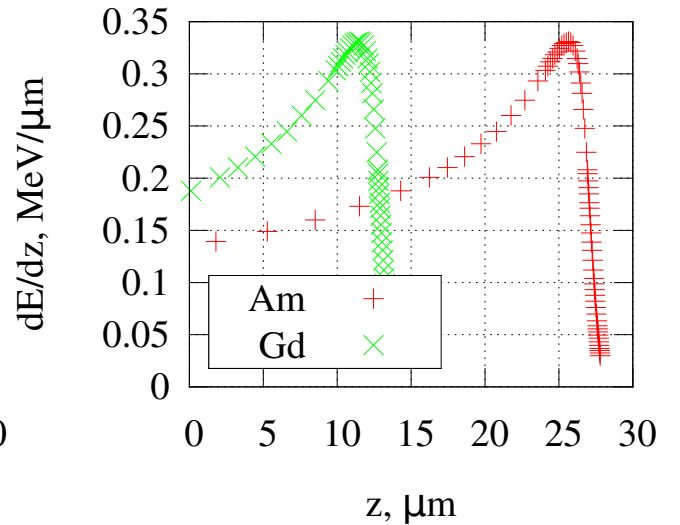


(d) Time dependence of the ratio of the gain measured with both ^{241}Am and ^{148}Gd sources to the nominal gain measured with only the ^{241}Am source for **B2D** polarimeter.

Figure 5: Comparison of the effective detector gains calculated with either one or both α -sources for the polarimeters equipped with two alpha sources. Outliers are not shown on the plots. Colors represent individual detectors.

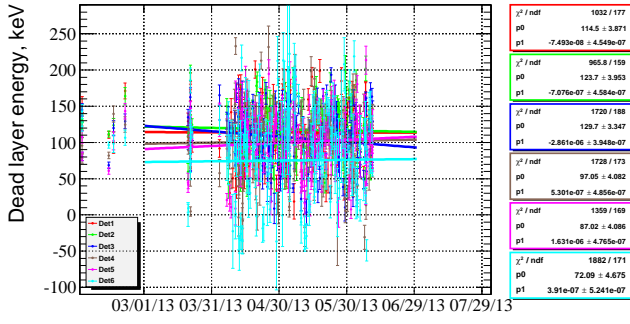


(a) CSDA versus alpha particle energy

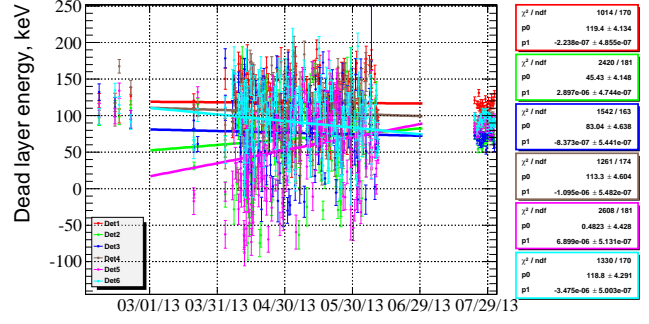


(b) Stopping power versus penetration depth

Figure 6

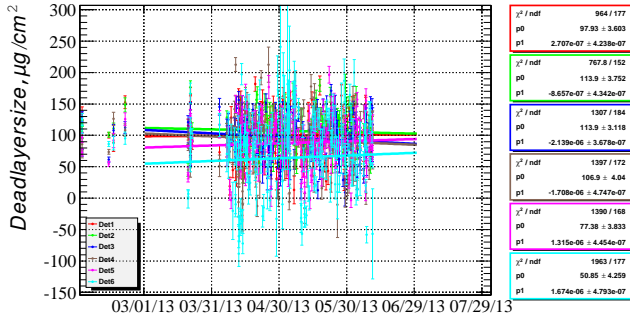


(a) B2D

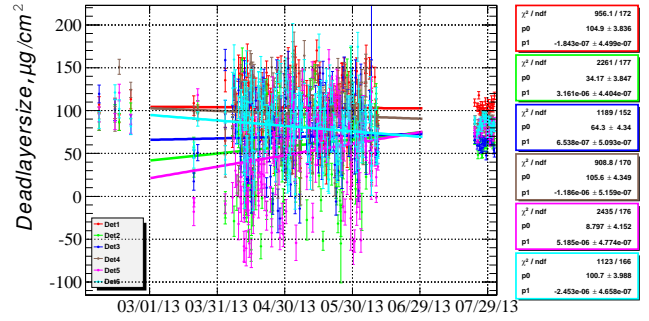


(b) Y2U

Figure 7: E_{DL} (see Figure 1) is the missing energy value extracted from linear fit of the americium and gadolinium points. Cut to remove outliers was applied to this plot.

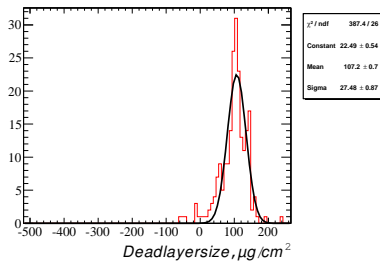


(a) B2D

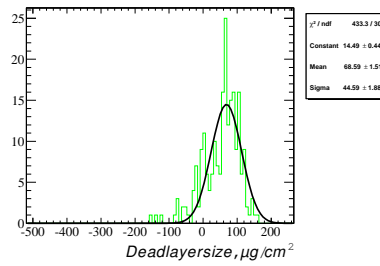


(b) Y2U

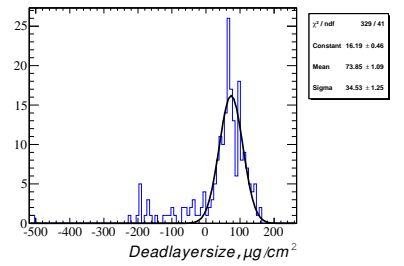
Figure 8: x_{DL} is the dead layer thickness calculated using formula (3). Cut to remove outliers was applied to this plot.



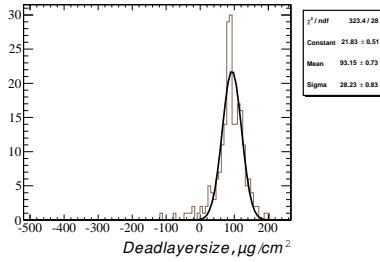
(a) Det1



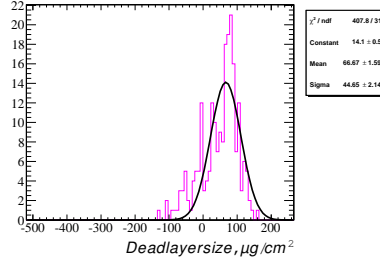
(b) Det2



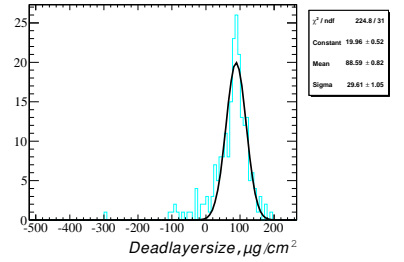
(c) Det3



(d) Det4



(e) Det5



(f) Det6

Figure 9: x_{DL} distribution in the measurements for Y2U.

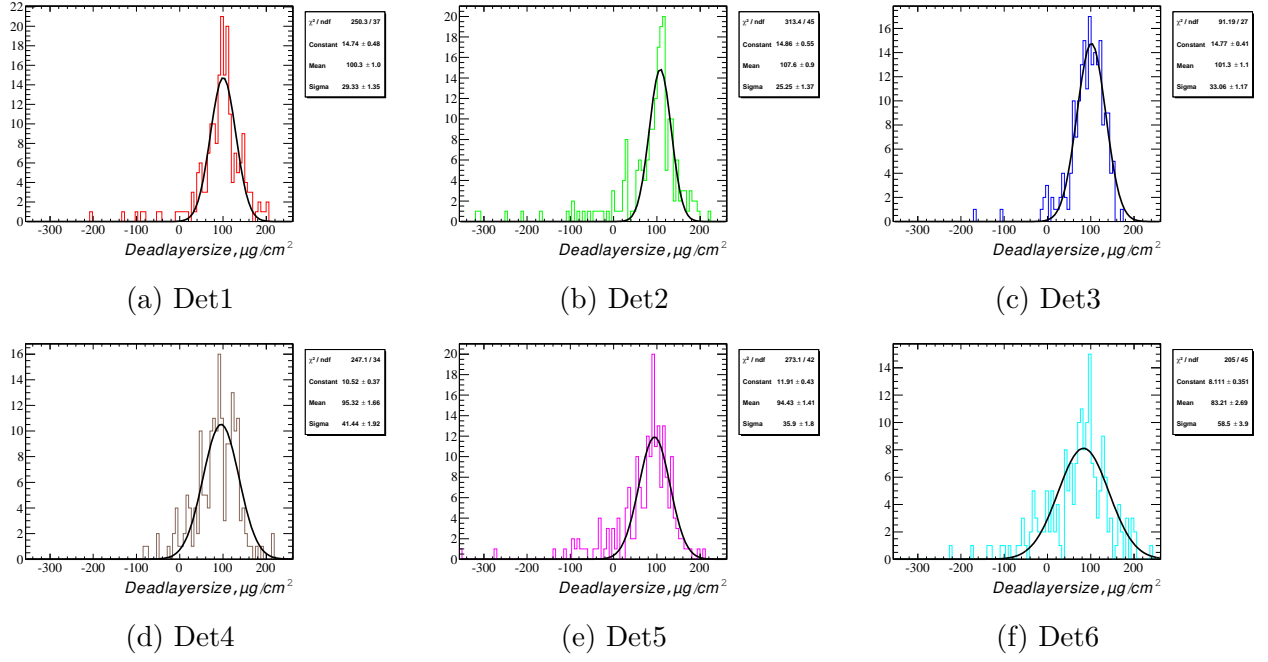


Figure 10: x_{DL} distribution in the measurements for B2D.

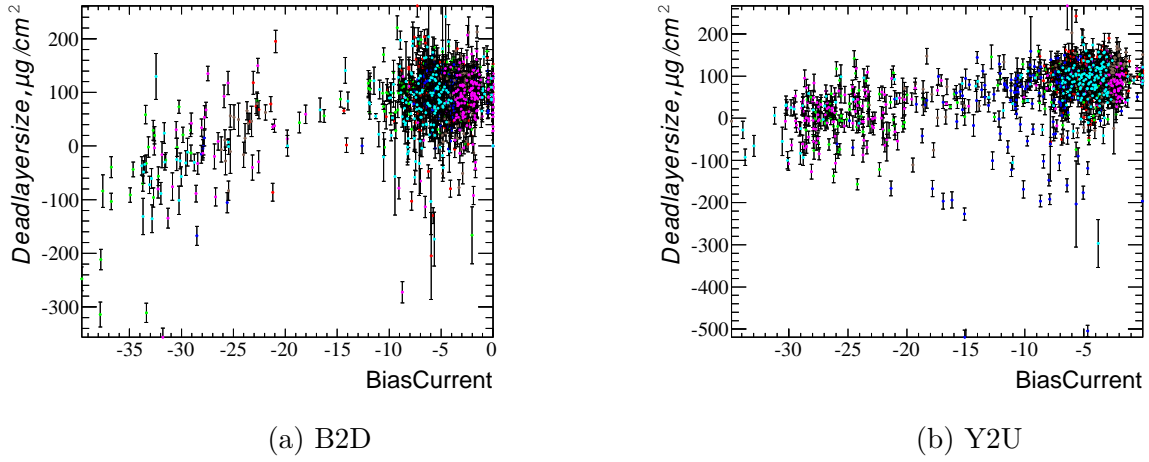
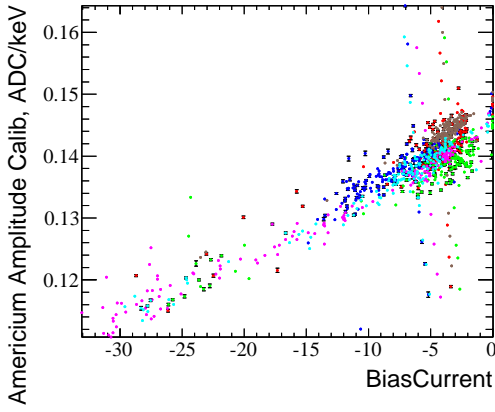
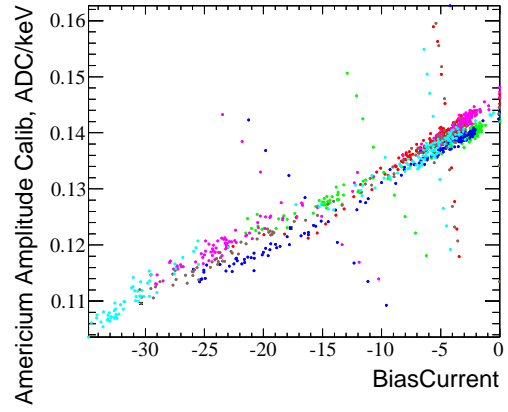


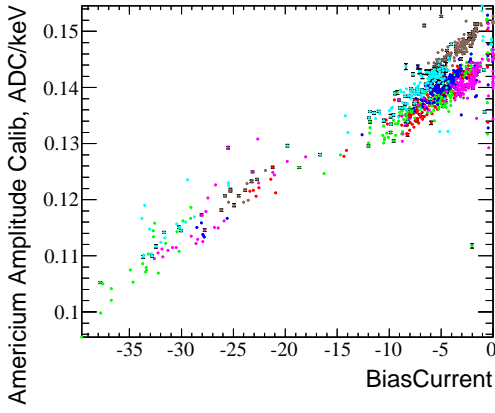
Figure 11: Bias current versus dead layer size dependency.



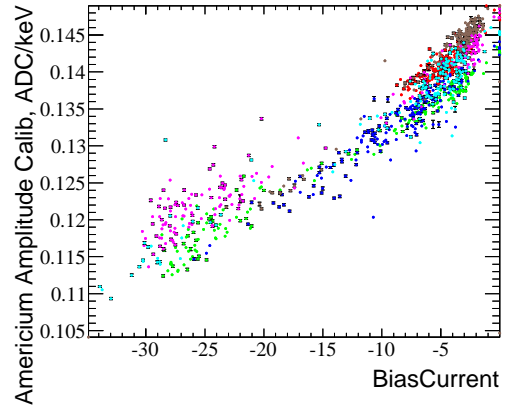
(a) B1U



(b) Y1D

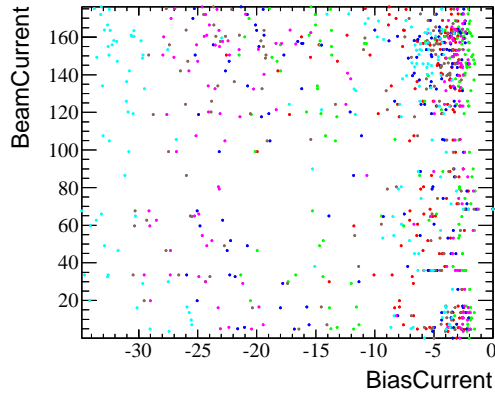


(c) B2D

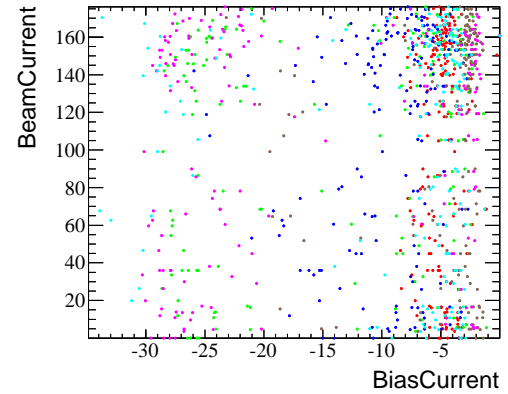


(d) Y2U

Figure 12: Bias current versus americium gain ($E_{\text{Am}}/\mu_{\text{Am}}$) dependency. The colors represent different detectors.



(a) Y1D



(b) Y2U

Figure 13: The average bias current during an alpha measurement versus the average beam intensity in the preceding store. The colors represent different detectors.

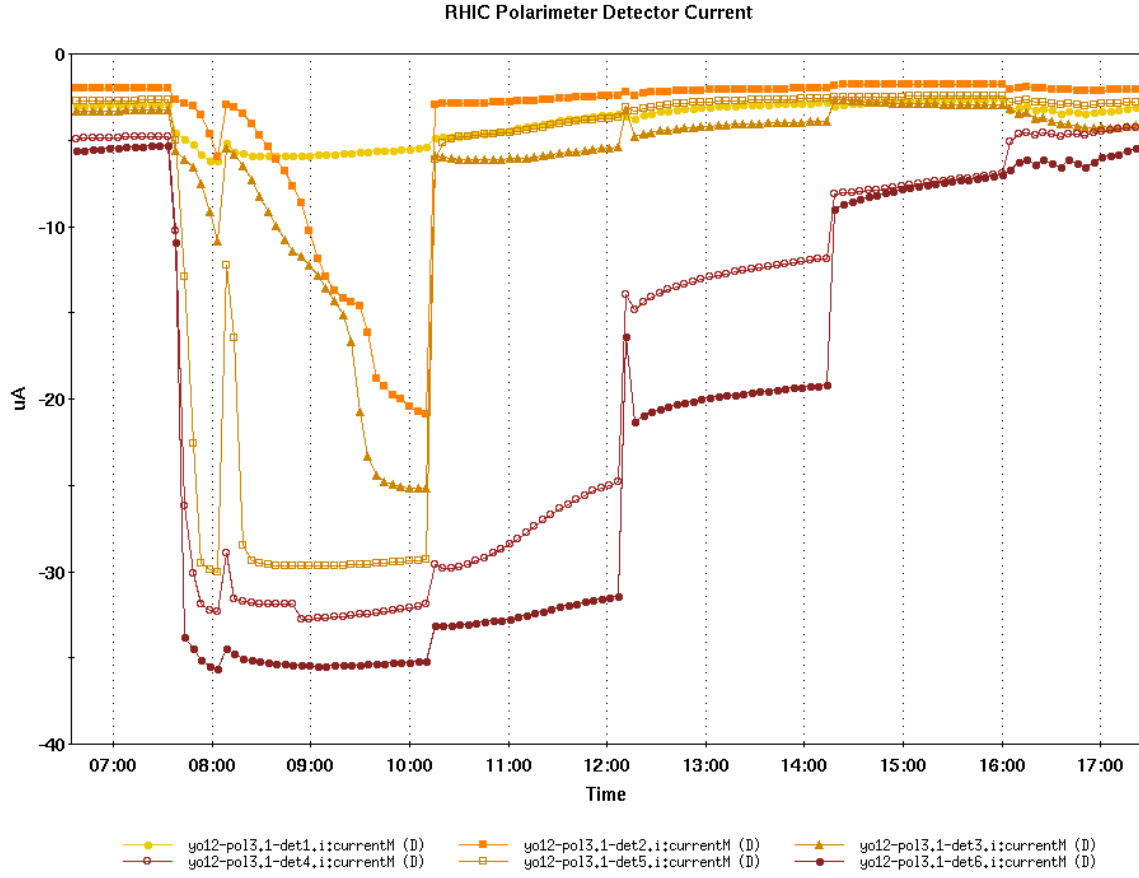
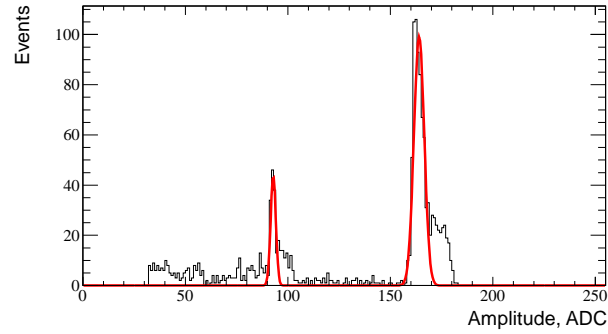
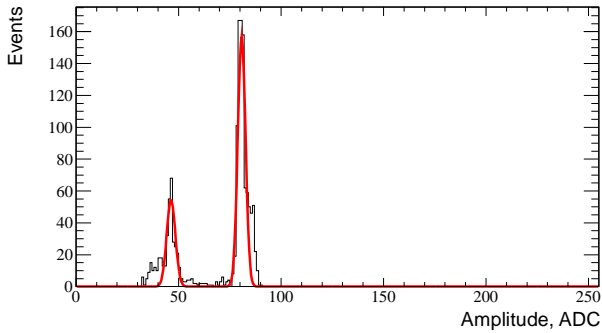


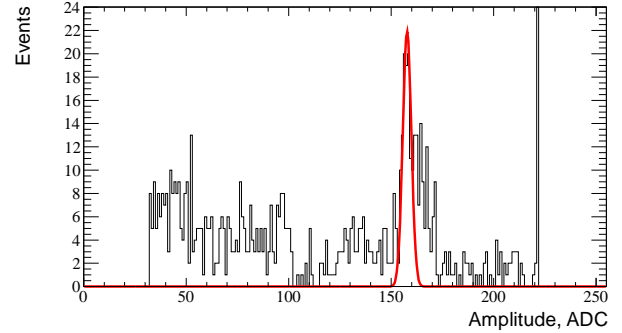
Figure 14: Bias current variation in Y1D detector during fill 17384. Some jumps coincide with polarization measurements.



(a) Signal attenuated to 1/5



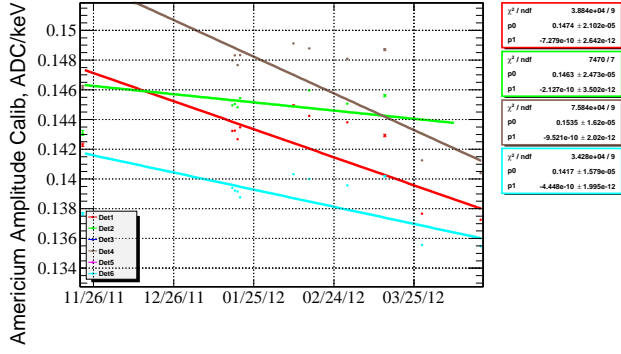
(b) Signal attenuated to 1/10



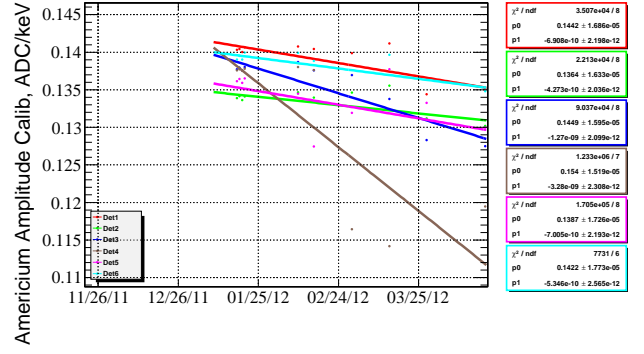
(c) Signal attenuated to 1/3

Figure 15: Alpha peaks as seen with different on-board attenuator settings (Y2U).

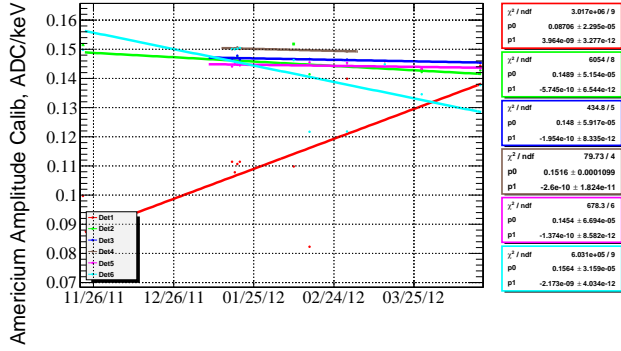
A Appendix: Run12 plots



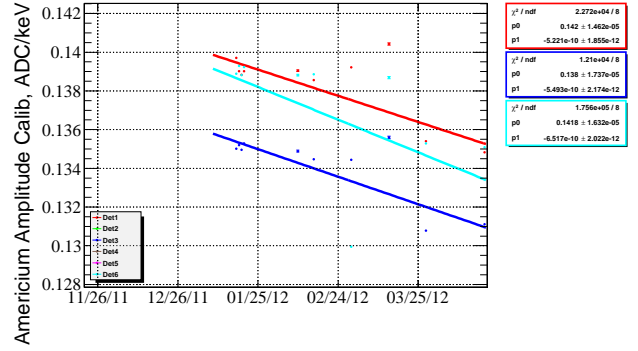
(a) B1U



(b) Y1D

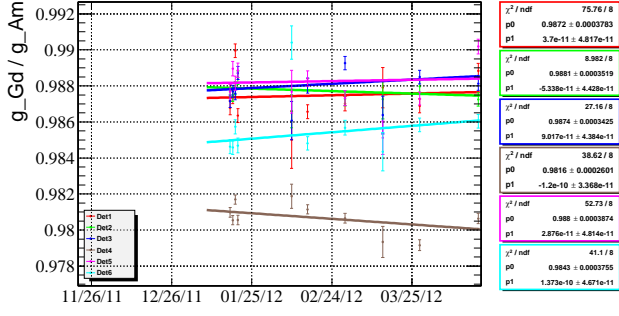


(c) B2D

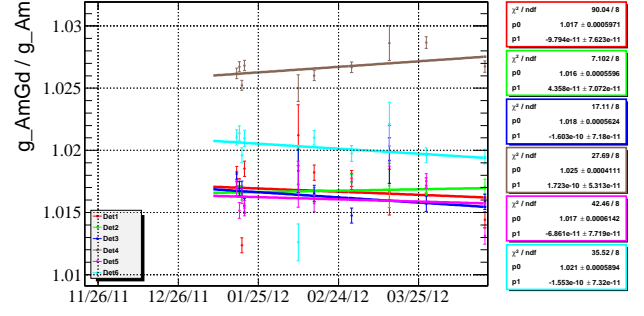


(d) Y2U

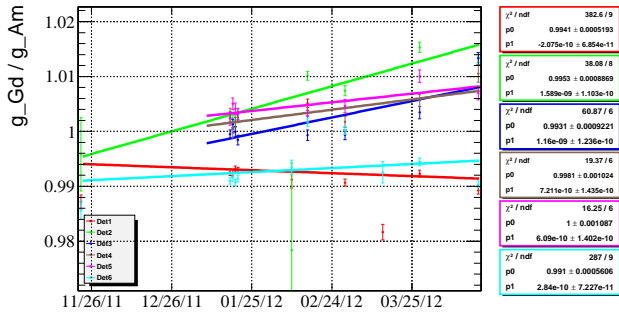
Figure 16: Time dependence of the detector gain g_{Am} as measured with α -particles emitted by the ^{241}Am source. Colors represent individual detectors. (run12_alpha)



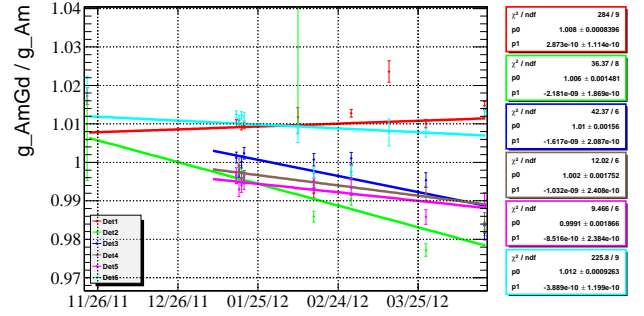
(a) Relation of gadolinium and americium gains for **Y2U** polarimeter.



(b) Relation of two-point (americium and gadolinium) linear fit slope and americium gain for **Y2U** polarimeter.

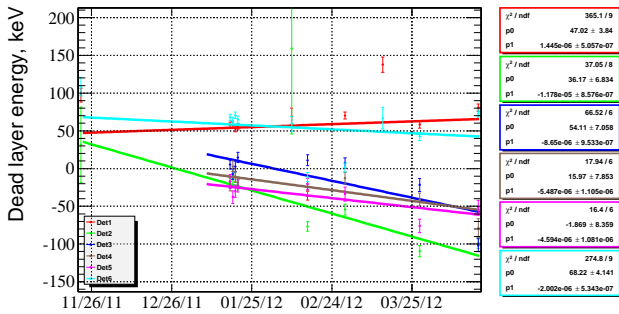


(c) Relation of gadolinium and americium gains for **B2D** polarimeter.

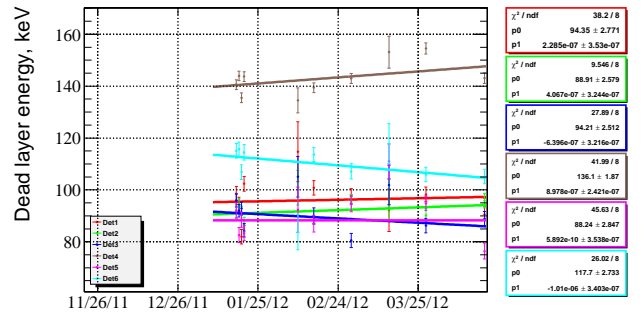


(d) Relation of two-point (americium and gadolinium) linear fit slope and americium gain for **B2D** polarimeter.

Figure 17: Comparison of the effective detector gains calculated with either one or both α -sources for the polarimeters equipped with two alpha sources. Outliers are not shown on the plots. Colors represent individual detectors. (run12_alpha)

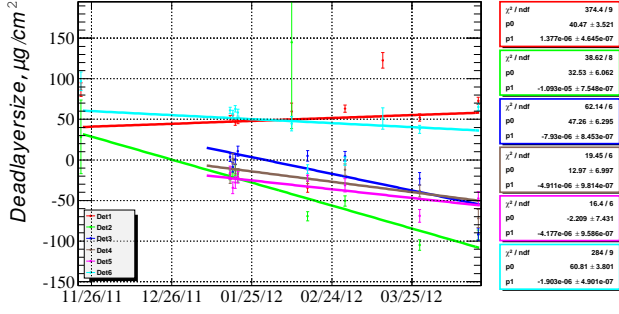


(a) B2D

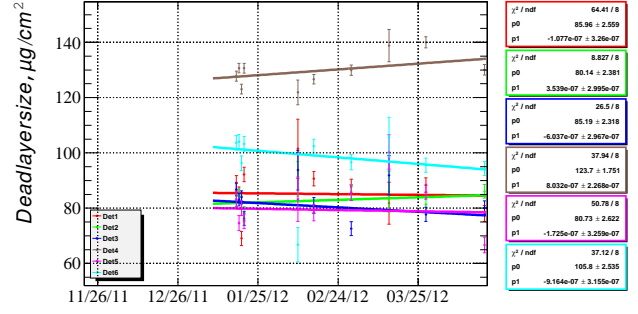


(b) Y2U

Figure 18: E_{DL} (see Figure 1) is the missing energy value extracted from linear fit of the americium and gadolinium points. Cut to remove outliers was applied to this plot. (run12_alpha)

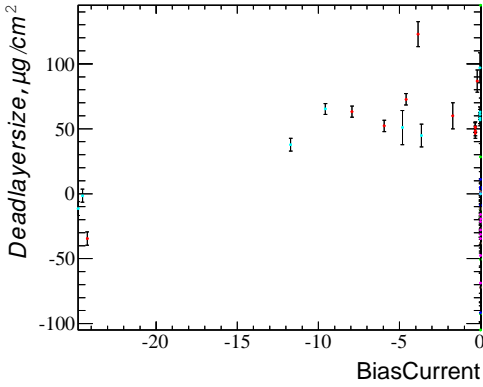


(a) B2D

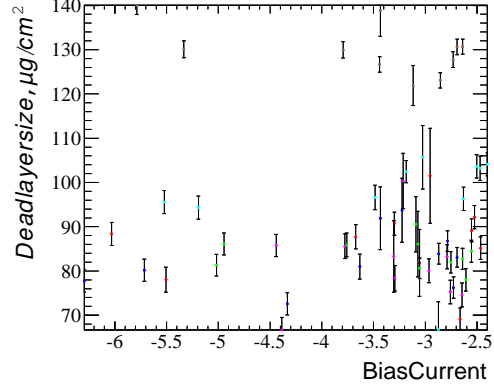


(b) Y2U

Figure 19: x_{DL} is the dead layer thickness calculated using formula (3). Cut to remove outliers was applied to this plot. (run12_alpha)

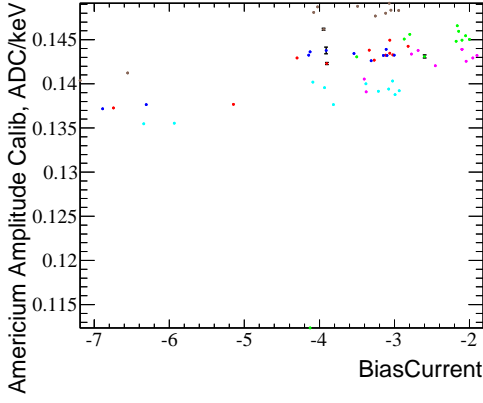


(a) B2D

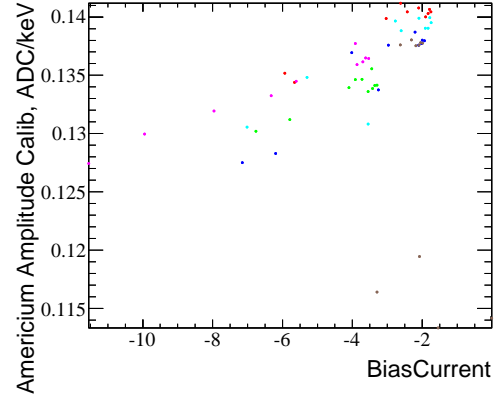


(b) Y2U

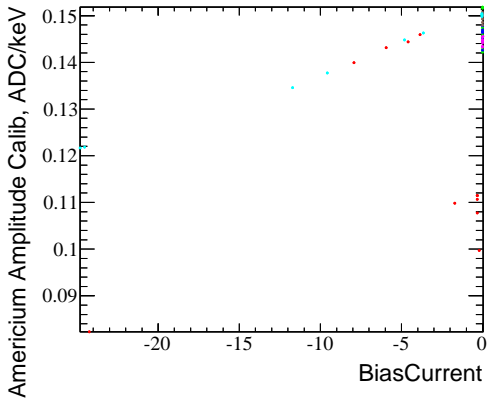
Figure 20: Bias current versus dead layer size dependency. (run12_alpha)



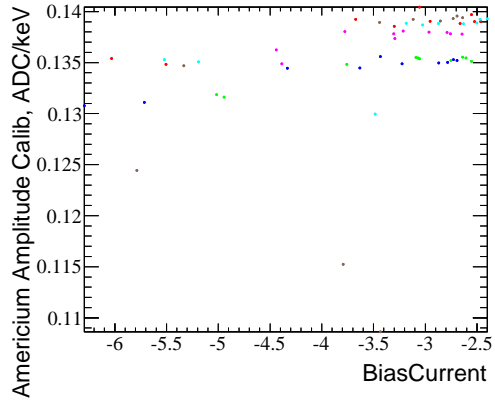
(a) B1U



(b) Y1D



(c) B2D



(d) Y2U

Figure 21: Bias current versus americium gain (E_{Am}/μ_{Am}) dependency. The colors represent different detectors. (run12_alpha)

References

- [1] RHIC polarimetry analysis framework: <https://github.com/rhicspin/cnipol>
- [2] A. Rytz, *At. Data and Nucl. Data Tables* **47**, 205 (1991).
- [3] ASTAR database. Stopping power and range tables for helium atoms: <http://physics.nist.gov/PhysRefData/Star/Text/ASTAR.html>
- [4] B. Schmidke, *Carbon & alpha E-deposition in Si*, July 8 (special meeting) https://wiki.bnl.gov/rhicspin/upload/7/72/Schmidke_Special_meeting_08.07.13.pdf
- [5] RHIC polarimetry results: <http://www.phy.bnl.gov/cnipol/rundb/>